ACS APPLIED NANO MATERIALS

www.acsanm.org Article

Cu_2O Cubes Decorated with Azine-Based Covalent Organic Framework Spheres and Pd Nanoparticles as Tandem Photocatalyst for Light-Driven Degradation of Chlorinated Biphenyls

Ahmed E. ElMetwally, Elnaz Zeynaloo, Dharmendra Shukla, Bapurao Surnar, Shanta Dhar, Joshua L. Cohn, Marc R. Knecht, and Leonidas G. Bachas*

Cite This: *ACS Appl. Nano Mater.* 2021, 4, 2795−2805 Read Online

ACCESS | Metrics & More | Article Recommendations | Supporting Information

ABSTRACT: Covalent organic frameworks (COFs) are promising candidates for heterogeneous photocatalytic reactions, though highly efficacious semiconductor−metal assemblies are often required to foster their photocatalytic performance. Herein, we report an efficient photocatalytic hybrid material that involves loading azine-based COF spheres onto Cu_2O cubes and decorating them with palladium nanoparticles. The photocatalytic performance of the material was studied via the light-driven degradation of chlorinated biphenyls. The Cu_2O-ACOF-1@Pd system demonstrated an outstanding performance over the bare Cu_2O or ACOF-1, which can be attributed to the synergistic effect induced by the multicomponent tandem photocatalyst. It is shown that for monochlorinated biphenyls, the congener with a chlorine atom in the para position is more vulnerable to degradation than its meta and ortho counterparts because of electronic effects and being less sterically hindered. Moreover, the presence of a chlorine atom in the para position as an electron donor increases the conjugation between the phenyl rings, which in turn increases the driving force for planarity that facilitates the removal of the chlorine atom. This trend could be attributed to the reactivity of superoxide radicals toward the different congeners of monochlorinated biphenyls. The data revealed that nucleophilic substitution occurring at the para position is characterized by the lowest Gibbs free energy, while that occurring at the ortho position is characterized by the highest Gibbs free energy.

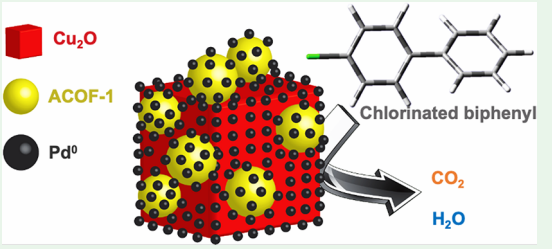

KEYWORDS: *covalent organic frameworks, metal oxide, photocatalysis, degradation, chlorinated biphenyls*

INTRODUCTION

Polychlorinated biphenyls (PCBs) are a group of manmade chlorinated compounds composed of two benzene rings linked together via a carbon−carbon bond. Chlorine atoms can replace up to 10 hydrogen atoms across the two benzene rings, resulting in up to 209 unique compounds. Non-ortho-substituted PCBs are deemed to be coplanar congeners, while the others are deemed nonplanar, where this is an indication of the ability of the rings to twist but not to completely turn. Moreover, the singly ortho-substituted congener is a polar molecule that is capable of forming hydrogen bonds. On the other hand, the meta- and para-substituted congeners are nonpolar and more lipophilic. PCB production dates back to the late 1920s, and they have been extensively used as lubricants and coolants in electrical apparatuses because of their resistance to combustion. They have been also used in paints, pesticides, adhesives, inks, coatings, and plasticizers.[1] PCBs can be released to the environment as a result of leakage from outdated electrical systems or disposal of industrial waste. PCB exposure via ingestion or inhalation is considered a serious risk to human health.[2,3] Notably, PCBs are relatively insoluble in water except for some ortho-substituted congeners, with the singly ortho-substituted congener having a maximum solubility of 25.6 μM. The solubility of the chlorinated congeners decreases when the ortho position becomes vacant and specifically when the para position becomes occupied as it intervenes with hydrogen bonding. Despite the fact that the production of PCBs was banned in 1979, they still exist in many pre-1979 products, and their disposal leads to accumulation in the environment.[4] Thus, the development of an efficient method to remediate contaminated wastewater is highly desirable. Photocatalysis may prove to be one of the most effective approaches for persistent organic contaminant remediation, where the development of different photoactive materials has been one of the most explored topics.[3,5,6] Recently, research has been focused beyond traditional semiconductors and toward metal-

Received: December 23, 2020
Accepted: March 8, 2021
Published: March 16, 2021

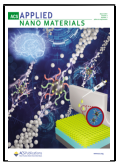

https://doi.org/10.1021/acsanm.0c03425
ACS Appl. Nano Mater. 2021, 4, 2795−2805

free, visible-light photocatalysts such as covalent organic frameworks.

Covalent organic frameworks (COFs) are a new class of porous crystalline materials that are made up of organic building units.[7,8] COFs have attracted the attention of scholars because of their unique properties such as adjustable shape, size, and pore type, where their functionality and structure are customizable through a sophisticated design of their building units.[7,9−13] COFs have also been exploited in various applications including separation and adsorption of gas molecules such as carbon dioxide, methane, and hydrogen, because of their adjustable composition, low density, and high surface area.[9−12,14] Further, COFs have been introduced as promising catalysts for different heterogeneous photocatalytic reactions.[14−17] Their efficient charge separation and charge transport can be attributed to the π-stacked structure of COFs.[18] Recently, azine-based COFs have been proven effective as photocatalysts in H_2O splitting.[19] Despite the exceptional photocatalytic performance of COFs, further improvement of their photocatalytic properties remains necessary to address challenging light-driven reactions. The π-electron conjugation in-plane, together with the possibility of axial charge transport in the stacking direction by the overlap of π-orbitals, can result in high charge carrier mobilities, thus making azine-based COFs promising supramolecular architectures for efficient light harvesting and charge transport. To boost the photocatalytic performance, COFs can be loaded with nanomaterials that are capable of enhancing charge separation, which in turn reduces the chances of electron/hole recombination.[20] Furthermore, the synergy between COFs and nanomaterials can markedly enhance the photocatalytic performance.

Herein, we provide a new strategy to foster the photocatalytic performance of a traditional semiconductor like Cu_2O by loading it with an azine-based COF (ACOF-1). In addition, decoration of the photocatalyst with palladium nanoparticles facilitates photoinduced charge separation that, in turn, enhances the photocatalytic activity. To our knowledge, this is the first report that describes the preparation of such ternary-type COF-based structures for photocatalysis. In the present work, ACOF-1 was prepared using an ultrasonically assisted method and characterized using Fourier transform infrared spectroscopy (FTIR), cross-polarization/magic angle spinning nuclear magnetic resonance (CP-MAS NMR), X-ray diffraction (XRD), Brunauer−Emmett−Teller (BET) surface area analysis, diffuse reflectance spectroscopy (DRS), scanning electron microscopy (SEM), and transmission electron microscopy (TEM). Next, the prepared ACOF-1 spheres were loaded onto Cu_2O cubes and then decorated with palladium nanoparticles. The prepared photocatalyst was characterized using SEM, TEM, XRD, FTIR, BET, diffuse reflectance spectroscopy (DRS), X-ray photoelectron spectroscopy (XPS), and inductively coupled plasma mass spectrometry (ICP-MS), followed by evaluation of the photocatalytic performance of the different materials in the light-driven degradation of chlorinated biphenyls. Radical trapping experiments were conducted to investigate the photocatalytic mechanism. The mineralization extent was monitored using total organic carbon (TOC) analysis, while GC−MS was used to detect any conceivable intermediates. The photocatalytic behavior of the Cu_2O-ACOF-1@Pd system demonstrated an outstanding performance, which can be attributed to the synergistic effect induced by the multi-component tandem photocatalyst. These findings reveal insights into the development and design of photoactive materials with an enhanced performance and how these materials influence the reaction kinetics of different photocatalytic systems.

EXPERIMENTAL SECTION

Materials. 1,3,5-Triformylbenzene and palladium acetate were obtained from Acros Organics. Hydrazine anhydrous, dioxane, copper sulfate pentahydrate, polyvinylpyrrolidone (average MW ∼29,000), sodium citrate tribasic dihydrate, 2-chlorobiphenyl (PCB 1), 3-chlorobiphenyl (PCB 2), 4-chlorobiphenyl (PCB 3), sodium carbonate, and Nafion 117 solution ∼5% (w/v) in a mixture of lower aliphatic alcohols and water were obtained from Sigma-Aldrich. Tetrachloro-*m*-xylene (TCMX) was obtained from AccuStandard. Ethylenediaminetetraacetic acid (EDTA) disodium salt, isopropanol, and *p*-benzoquinone were purchased from Alfa Aesar. Milli-Q water (18.2 MΩ·cm) was used for all experiments. Absolute ethanol was purchased from Pharmco-Aaper.

METHODS

Ultrasonically Assisted Preparation of ACOF-1. ACOF-1 was prepared using an amended version of the procedure described elsewhere.[21] In particular, a 60 mL borosilicate glass vial with a silicone septum cap was filled with 1,3,5-triformylbenzene (240 mg), dioxane (8 mL), and acetic acid (800 μL, 6 M). The glass vial was tightly sealed, flushed with argon for 10 min, and sonicated for 10 min. Next, hydrazine hydrate (93 μL) was injected into the glass vial using a syringe under ultrasonic irradiation. At this point, a pale yellow solid was formed at the bottom of the glass vial as shown in Scheme S1. After the addition of hydrazine, the glass vial was sonicated for 15 min, and then the glass vial was immersed in an oil bath at 120 °C for 72 h. The resulting pale yellow solid was collected by centrifugation and washed with dioxane followed by tetrahydrofuran and acetone and subsequently dried overnight *in vacuo* at 60 °C.

Preparation of Cu_2O-ACOF-1. The prepared ACOF-1 (0.1 g) was dispersed in 210 mL of copper sulfate solution (0.032 M in water), and the resulting slurry was sonicated for 5 min to ensure complete dispersion of the ACOF-1 particles. Next, 3.0 g of polyvinylpyrrolidone was added, and the mixture was kept under stirring for 15 min. Following this, 40 mL of aqueous sodium carbonate (0.61 M) and sodium citrate (0.37 M) was added dropwise under stirring. The slurry was kept under stirring for 15 min in a round-bottom flask, and then an aqueous glucose solution (1.4 M) was added dropwise. The round-bottom flask was then wrapped with aluminum foil to block the light and was immersed in an oil bath at 80 °C for 2 h under stirring. The resultant solids were separated by centrifugation, washed with DI water and acetone, and dried overnight *in vacuo* at 60 °C.

Preparation of Cu_2O-ACOF-1@Pd. Pd^0 was deposited on Cu_2O-ACOF-1 via galvanic replacement as described in our previous report.[22] The prepared Cu_2O-ACOF-1 (0.2 g) was sonicated in 140 mL of absolute ethanol for 10 min to ensure complete dispersion of the particles, and then 2.70 mL of ethyl acetate containing 28 mg of palladium acetate was added to the mixture. The flask was wrapped with aluminum foil to block the light, and the mixture was kept overnight while stirring. Eventually, the obtained solids were separated, washed, and dried *in vacuo* at 60 °C. ACOF-1@Pd and Cu_2O@Pd were prepared using the same preparation method.

Characterization. The XRD patterns of the prepared materials were obtained on a PANalytical, X'Pert Pro MPD using Cu Kα radiation. A Shimadzu model UV-2600 system was used for UV−vis DRS analysis. A PerkinElmer FTIR (Frontier) spectrometer was used to obtain FTIR spectra of the prepared materials. Solid-state ^{13}C CP/MAS NMR spectra were obtained on a Bruker Avance III 400 WB spectrometer. A JEOL JEM-1400 TEM operating at 80 kV was used to obtain the TEM images. The sample was prepared by dispersing 5

https://doi.org/10.1021/acsanm.0c03425
ACS Appl. Nano Mater. 2021, 4, 2795−2805

mg of each material in 200 μL of absolute ethanol using ultrasonic irradiation. Next, 5 μL of the dispersed material was drop-casted onto a carbon-coated 400 mesh copper grid. A Philips XL30 field-emission environmental SEM equipped with an Oxford energy-dispersive X-ray detector was employed to obtain the SEM images. For sample preparation, 5 mg of each material was dispersed in 200 μL of absolute ethanol using ultrasonic irradiation. Next, 50 μL of the dispersed material was drop-casted on an aluminum specimen mount. Surface area analysis was performed on an Autosorb-iQ system (Quantachrome Instruments). X-ray photoelectron spectroscopy (XPS) analysis was carried out using a Kratos Axis UltraDLD XPS system equipped with an Al X-ray source and a 165 mm mean radius electron energy hemispherical analyzer. An Agilent 7900 inductively coupled plasma mass spectrometer was employed for elemental analysis of the prepared materials. Photoluminescence (PL) spectra were recorded on a Fluorolog (Horiba Jobin Yvon) spectrometer.

Photocatalytic Degradation of Chlorinated Biphenyls. For each photocatalytic run, a 50 mL quartz beaker was filled with 50 mL of specific PCB congener solution (7 μM in water) to which 10 mg of the catalyst was dispersed using an ultrasonic bath for 30 s. The quartz beaker was placed at a distance of ∼10 cm in front of a solar simulator (Oriel Instruments, Newport Corporation) with a high-power mercury−xenon lamp (300 W). During each experiment, aliquots (500 μL) were withdrawn at preset time intervals and mixed with hexane (500 μL) for extraction of unreacted PCBs and PCB degradation intermediates. Next, the hexane extract (100 μL) was combined with 10 μL of TCMX (10 ppm) as an internal standard and analyzed using GC/MS (Agilent 5975C equipped with HP-5MS column: 30 m length, 0.25 μm film thickness, 0.250 mm ID). For trapping experiments, isopropanol (10 mM in water), *p*-benzoquinone (1 mM in water), and EDTA (5 mM in water) were used. The extent of mineralization was monitored on a TOC analyzer (Shimadzu TOC-L).

Electrochemical Analyses. Electrochemical measurements were conducted in a three-electrode cell with Pt as a counter electrode and Ag/AgCl (3 M NaCl) as a reference electrode. For the working electrode, fluorine-doped tin oxide (FTO) glass was used as a substrate for deposition of the materials being investigated. Prior to the deposition of the active materials, the FTO glass was sonicated in ethanol for 30 min and then dried *in vacuo* at 60 °C. For electrochemical impedance spectroscopy (EIS) measurements, the active material was deposited using a drop-casting method on FTO glass with an active area of 1 cm^2, where 5 mg of the active material was dispersed in 10 mL of 50/50 (v/v) ethanol/water mixture using a bath sonicator. Next, 100 μL of the mixture was dropped onto the FTO glass and dried at 100 °C for 60 min. This step was repeated three times to obtain the desired thickness. The impedance spectra measurements were conducted over the frequency range from 100 kHz to 0.1 Hz. For photocurrent measurements, the active area on FTO glass was 0.5 cm^2, where 40 mg of the material was dispersed in 400 μL of ethanol containing 1% Nafion (v/v) using a bath sonicator, and then 10 μL of the mixture was dropped onto the FTO glass and air dried. The EIS measurements were conducted in the dark using an aqueous electrolyte solution of 0.1 M KCl and 5 mM $K_3[Fe(CN)_6]$, while a 0.2 M Na_2SO_4 aqueous solution was used during the photocurrent measurements. A solar simulator (Oriel Instruments, Newport Corporation) with a high-power mercury−xenon lamp (300 W) was employed as a light source. The data were collected using an electrochemical workstation PARSTAT 2273 with PowerSuite software version 2.40 (EG&G Princeton Applied Research, Oak Ridge, TN).

RESULTS AND DISCUSSION

Material Synthesis, Integration, and Characterization. ACOF-1 was prepared through a modified ultrasonic-assisted approach, where the condensation reaction of 1,3,5-triformylbenzene with hydrazine hydrate (Scheme 1) under ultrasonic irradiation led to the formation of spherical particles with a well-defined shape (Figure 1).

Scheme 1. Synthesis of ACOF-1

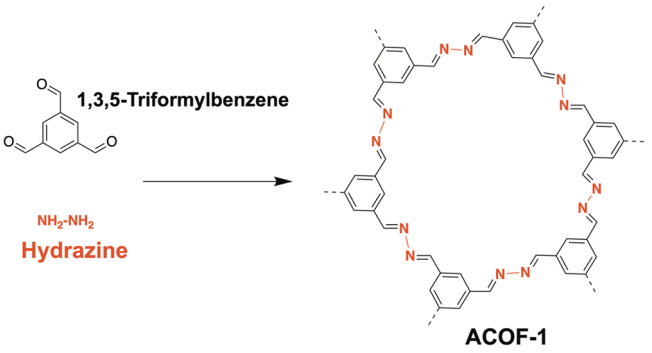

Ultrasonic irradiation enhances the nucleation rate and reduces the metastable zone and induction time, which leads to the formation of smaller crystals with more defined shapes when compared with conventional preparation methods.[21]

To validate the structure of the prepared ACOF-1, the sample was characterized using FTIR, solid-state ^{13}C cross-polarization/magic angle spinning (CP-MAS) NMR, XRD, DRS, and BET analysis. The FTIR spectrum of ACOF-1 (Supporting Information, Figure S1) shows a typical stretching band at 1623 cm^{-1} that is ascribed to the stretching vibrations of the C═N bond. Moreover, the disappearance of the band at 1700 cm^{-1} that corresponds to the carbonyl group of the 1,3,5-triformylbenzene is an evidence for the absence of any unreacted substrate in the ACOF-1 material. The ^{13}C CP-MAS NMR spectrum of the prepared ACOF-1 shows a peak at 161 ppm that arises from the C═N bond, while there is no trace for the carbonyl carbon of the 1,3,5-triformyl benzene as shown in the Supporting Information (Figure S2). The XRD pattern of ACOF-1 (Supporting Information, Figure S3) shows 2θ peaks at 6.9, 12, and 18.8° that correspond to the (100), (110), and (120) facets of ACOF-1, respectively, while the peak that appears at 26.9° corresponds to π-π stacking between COF layers and can be ascribed to the (001) plane. To assess the surface area of the prepared ACOF-1, N_2-sorption isotherm measurements were employed. Prior to analysis, degassing was carried out at 120 °C for 12 h. The obtained isotherm (Supporting Information, Figure S4) can be classified as a type I adsorption isotherm according to the International Union of Pure and Applied Chemistry (IUPAC) classification. The total specific surface area obtained using the BET equation is estimated to be 1134 m^2 g^{-1}. The DRS analysis (Supporting Information, Figure S5) shows that the prepared ACOF-1 has a band gap energy of 2.7 eV, suggesting that the material is photoactive in the visible region. Moreover, both the square and square root of absorption coefficient were plotted against energy (Supporting Information, Figure S5) to investigate the transition character of the sharp edge.[23−25] The linear $(\alpha h\nu)^{1/2}$ versus energy plot, in contrast to the deviated $(\alpha h\nu)^2$ versus energy plot, manifests that the absorption edge of ACOF-1 is caused by an indirect transition. In semiconductors with an indirect band gap, the excited electrons have to travel through a particular *k*-space distance to be transferred to the valence band, which diminishes the recombination probability of charge carriers.[23]

To foster the photocatalytic performance, ACOF-1 was loaded onto Cu_2O cubes, and this composite was subsequently decorated with Pd nanoparticles as shown in Scheme 2.

https://doi.org/10.1021/acsanm.0c03425
ACS Appl. Nano Mater. 2021, 4, 2795−2805

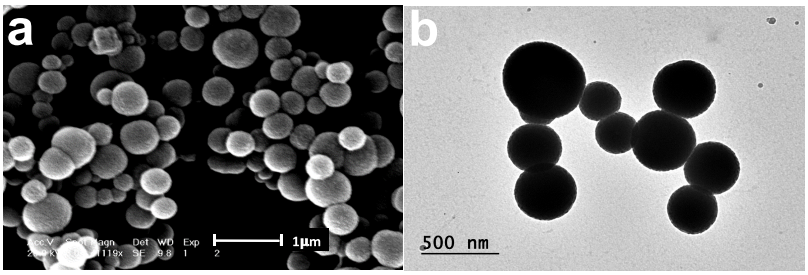

Figure 1. SEM image (a) and TEM image (b) of the prepared ACOF-1.

Scheme 2. Preparation of Cu_2O-ACOF-1@Pd

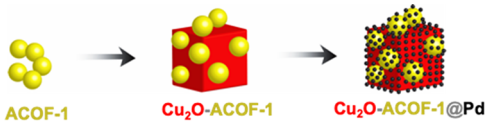

To investigate thoroughly the morphological effects upon loading of ACOF-1, SEM analysis was carried out. Figure 2a shows uniform cubes of the bare Cu_2O before loading of ACOF-1 spherical particles and Pd, while Figure 2b shows several spherical particles that lie on the surface of cubes. It is evident that the texture of the cubes and spheres is slightly rough, and this is due to the Pd sputter coating prior to SEM analysis as it is extremely difficult to get clear SEM images for ACOF-1 without sputter coating. For the same reason, imaging of the Cu_2O-ACOF-1@Pd using SEM is not possible, and thus TEM analysis was carried out. The TEM image of the bare Cu_2O (Figure 2c) presents the overall cubic architecture of cuprous oxide, while Figure 2d shows the cubes loaded with spheres for Cu_2O-ACOF-1. It is evident that the surface of the cubes and spheres is smooth prior to the deposition of Pd nanoparticles. On the other hand, the TEM images of Cu_2O-ACOF-1@Pd (Figure 2e,f) show numerous small particles deposited on both the cubes and spheres, which is indicative of the successful decoration of Cu_2O-ACOF-1 with Pd. ACOF-1@Pd and Cu_2O@Pd were also prepared for comparison, and their TEM images are displayed in the Supporting Information, Figure S6.

To assess the effectiveness of the employed preparation method, Cu_2O was mixed with ACOF-1 in a mortar. The SEM images (Supporting Information, Figure S7) show the ACOF-1 particles and Cu_2O cube prepared by physical mixing, and it is clear that spherical particles of ACOF-1 reside away from the cube, which elaborates the incapability of the physical mixing method for loading of ACOF-1 onto Cu_2O.

The XRD patterns of the prepared materials are displayed in Figure S3, where the diffraction pattern of Cu_2O-ACOF-1@Pd

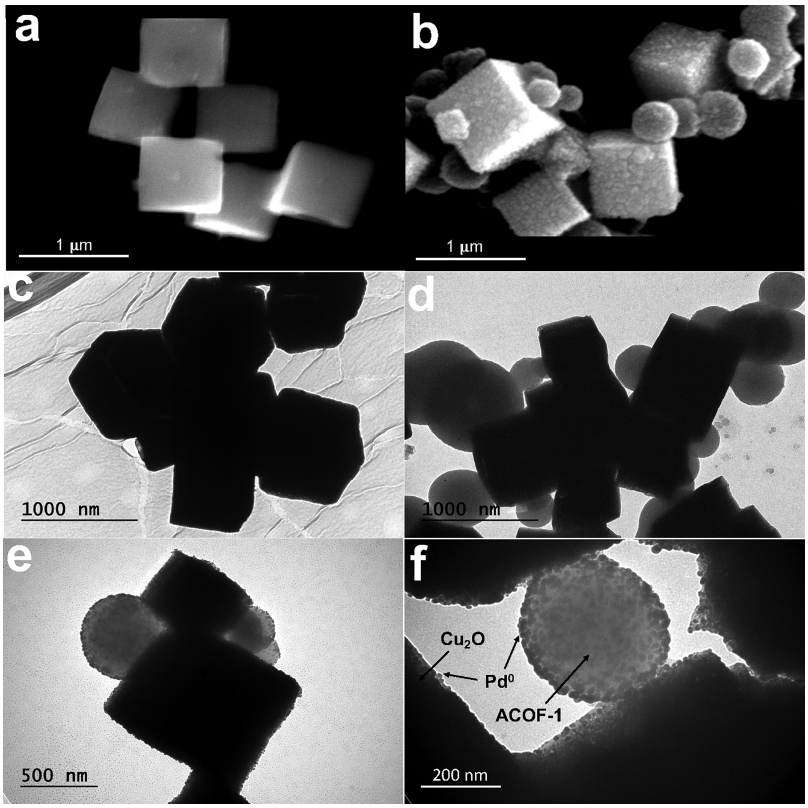

Figure 2. SEM images of (a) bare Cu_2O and (b) Cu_2O-ACOF-1; TEM images of (c) bare Cu_2O, (d) Cu_2O-ACOF-1, and (e,f) Cu_2O-ACOF-1@Pd.

https://doi.org/10.1021/acsanm.0c03425
ACS Appl. Nano Mater. 2021, 4, 2795−2805

was compared with that of Cu_2O and ACOF-1. The XRD pattern of Cu_2O-ACOF-1@Pd (Figure 3a) exhibits the

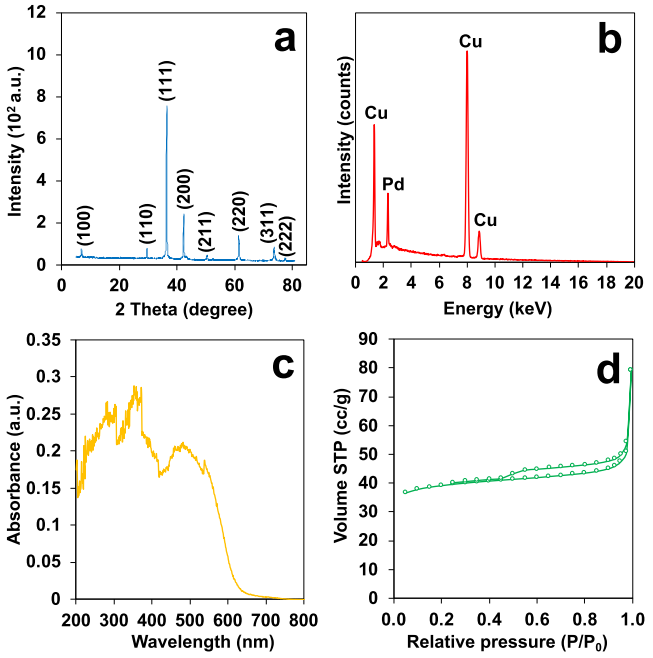

Figure 3. (a) XRD pattern of Cu_2O-ACOF-1@Pd, (b) EDS analysis of Cu_2O-ACOF-1@Pd, (c) DRS analysis of Cu_2O-ACOF-1@Pd, and (d) N_2 adsorption−desorption isotherm of Cu_2O-ACOF-1@Pd.

characteristic peaks of both ACOF-1 and Cu_2O, with a peak at 6.9°, confirming the presence of ACOF-1. The XRD pattern also displays reflections at 2θ = 29.6, 36.5, 42.4, 50.5 61.6, 73.9, and 77.7° that correspond to reflection planes of Cu_2O.[26] It is worth mentioning that there were no additional peaks observed, suggesting that the prepared material was free of Cu^0 and CuO. To validate and quantify the Pd content in the prepared composites, EDS analysis was carried out, and the obtained data are presented in Figure 3b.

The spectrum shows an intense peak at ∼2.8 keV that corresponds to the Lα X-ray line of palladium with a content of 6.6 ± 0.7 wt %. This content was also validated using inductively coupled plasma mass spectrometry (ICP-MS), which found it to be 6.1 wt %. The FTIR spectra of the prepared materials are displayed in the Supporting Information, Figure S8, where the bands of Cu_2O-ACOF-1@Pd were compared with those of Cu_2O-ACOF-1 and ACOF-1. The FTIR spectra of Cu_2O-ACOF-1@Pd and Cu_2O-ACOF-1 exhibit the characteristic bands of ACOF-1, which demonstrates that ACOF-1 was able to endure the preparation conditions of Cu_2O and Pd nanoparticles.

The DRS spectrum of the prepared Cu_2O-ACOF-1@Pd is displayed in Figure 3c. The prepared material shows a spectrum with an absorption edge at 620 nm, which indicates that the prepared photocatalyst can perform effectively in the visible region. For comparison purposes, the DRS spectrum of Cu_2O was analyzed, and the obtained data are presented in the Supporting Information, Figure S10. The plot of $(\alpha h\nu)^2$ versus energy was linear, while that of the $(\alpha h\nu)^{1/2}$ versus energy plot deviated from linearity; and this suggests that the absorption edge of Cu_2O is caused by direct transition (Supporting Information, Figure S9). The surface area analysis for Cu_2O-ACOF-1 and Cu_2O-ACOF-1@Pd was studied using nitrogen adsorption−desorption, and the data are displayed in the Supporting Information, Figure S4 and Figure 3d. The obtained isotherm shows a combination of type I and type II characters according to the IUPAC classification. The total specific surface areas of Cu_2O-ACOF-1 and Cu_2O-ACOF-1@Pd obtained using the BET equation are estimated to be 114 and 98 $m^2\ g^{-1}$, respectively.

To investigate the chemical state of Cu_2O-ACOF-1@Pd surface species, XPS analysis was conducted, and the obtained spectra are presented in Figure 4. The full spectrum of the

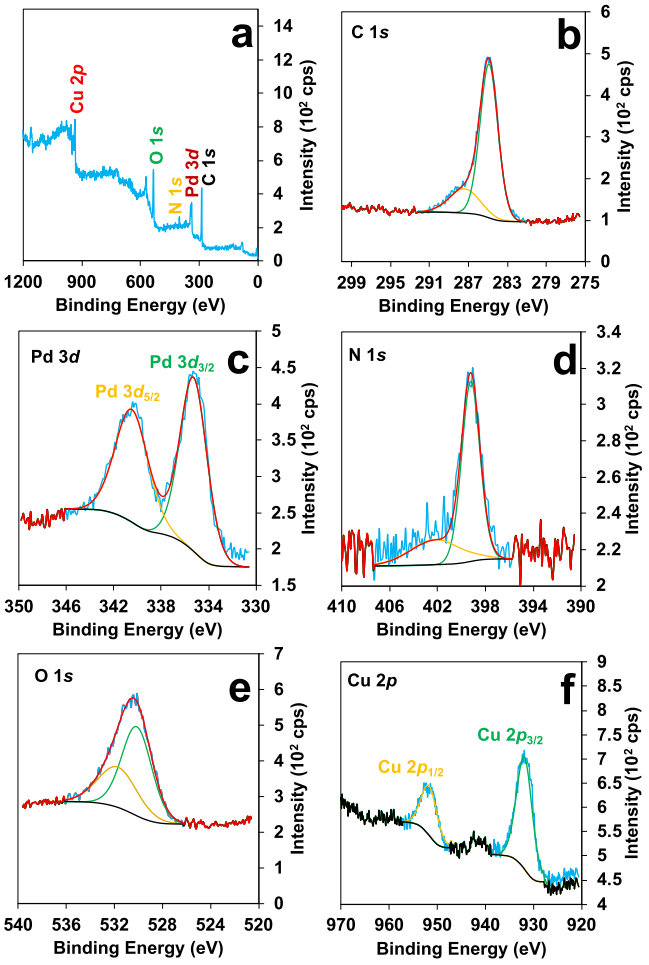

Figure 4. (a) Wide spectrum of Cu_2O-ACOF-1@Pd and high-resolution XPS spectra of (b) C 1s, (c) Pd 3d, (d) N 1s, (e) O 1s, and (f) Cu 2p.

Cu_2O-ACOF-1@Pd (Figure 4a) indicates that C, N, Cu, O, and Pd are present in the sample. The C 1s spectrum (Figure 4b) shows a peak at 284.8 eV, which is ascribed to the sp^2-bonded carbon of the ACOF-1 benzene ring.[27] The C 1s spectrum also shows a peak at 287.4 eV that corresponds to C═N of the azine linkage. For Pd 3d (Figure 4c), two peaks appear at 335.2 and 340.8 eV that are attributed to Pd $3d_{3/2}$ and $3d_{5/2}$, respectively. These peaks can be indexed to Pd^0, and no peaks were observed for Pd^{2+} or PdO.[22] On the other hand, the N 1s spectrum (Figure 4d) exhibits a peak at 399.5 eV that is assigned to C═N of the ACOF-1 azine linkage,[28] while the small peak observed at 403.1 eV is attributed to the N−N bond. Moreover, the O 1s spectrum (Figure 4e) shows two peaks at 530.1 and 531.7 eV that are assigned to O^{2-} of Cu_2O and surface-adsorbed O^- species, respectively.[29,30] The high-

https://doi.org/10.1021/acsanm.0c03425
ACS Appl. Nano Mater. 2021, 4, 2795−2805

resolution spectrum of Cu 2p (Figure 4f) shows two peaks centered at 931.6 and 951.5 eV that are ascribed to Cu $2p_{3/2}$ and Cu $2p_{1/2}$, respectively, which are consistent with the values reported for Cu^{1+}.[22]

Photocatalytic Activity. The photocatalytic activity of the prepared materials was tested using three different monochlorinated PCB congeners with chlorine at ortho, meta, or para positions. As anticipated, the chlorine position markedly affects the photocatalytic activity based on steric hindrance and electronic effects. For these experiments, a concentration of 7 μM was chosen for the three PCB congeners in water because the maximum solubility of the least soluble of the three congeners, PCB 3, is 7.1 μM.

Prior to the photocatalytic testing, adsorption experiments were conducted in the dark to estimate the adsorption capacity of the prepared materials because materials with a high surface area like ACOF-1 could have a high adsorption capacity. For all samples, the adsorption−desorption equilibrium was attained after 1 h of stirring in the dark; consequently, the material was allowed to equilibrate with the PCB substrate for 1 h in the dark before initiating any photocatalytic study. The obtained data presented in the Supporting Information, Figure S10 show that the adsorption capacity of the employed materials can be arranged as ACOF-1 > ACOF-1@Pd > Cu_2O-ACOF-1 > Cu_2O-ACOF-1@Pd. The decline in the adsorption capacity upon loading of Cu_2O can be attributed to the decrease in surface area, and this is consistent with the data obtained from BET analysis. For ACOF-1, the adsorptions of PCB 1, PCB 2, and PCB 3 reached 24, 27, and 28%, respectively, after 1 h of stirring in the dark.

To evaluate the effect of photolysis on the degradation of PCBs in the absence of any catalyst, 50 mL of each congener was illuminated with light (150 W), and the degradation extent was screened over time; the obtained data are presented in Figure 5. The data (referred to as a control in Figure 5) reveal that photolysis alone is incapable of degrading to a substantial degree in any of the tested congeners even after 1 h of illumination; and the observed degradations were 5, 10, and 10% for PCB 1, PCB 2, and PCB 3, respectively. The photocatalytic reactivity of the prepared materials was evaluated by dispersing 10 mg of each catalyst in 50 mL of congener solution, and the reaction medium was irradiated after reaching adsorption−desorption equilibrium. Figure 5 displays the photocatalytic degradation data of PCB 1, PCB 2, and PCB 3 using the prepared materials. The reaction kinetics was estimated and compared by monitoring the photocatalytic degradation of the different congeners over time.

For all the systems, Cu_2O-ACOF-1@Pd exhibits the best performance among the other tested catalysts, where the complete degradation of PCB 1, PCB 2, and PCB 3 was achieved after 40, 40, and 30 min, respectively. For the purposes of this article, we define complete degradation as the time it takes to reach a concentration of the parent compound that is below the detection limit of the analytical method used. The photocatalytic performance of the tested catalysts can be arranged as Cu_2O-ACOF-1@Pd > Cu_2O-ACOF-1 > ACOF-1@Pd > ACOF-1. It should be noted that no byproducts were observed on the GC−MS during the degradation of the different congeners of PCBs for any of the tested catalysts.

For the bare ACOF-1, the degradation extents reached 73, 82, and 84% for PCB 1, PCB 2, and PCB 3, respectively, after 60 min of irradiation, which is a high level of performance when compared with other metal-free semiconductors. Such

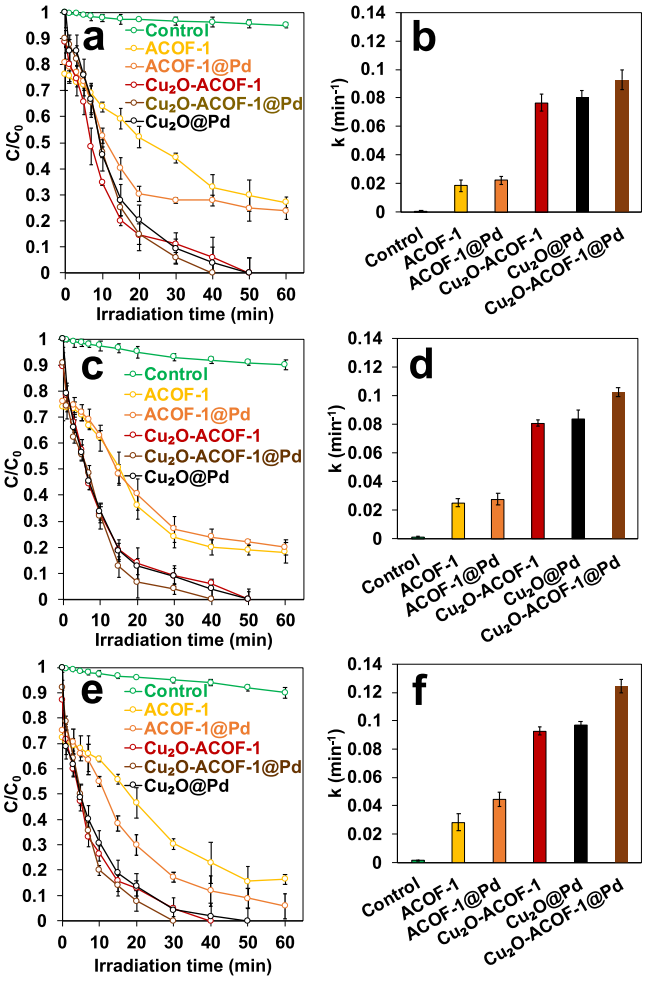

Figure 5. Photocatalytic degradation and pseudo-first-order rate constants of PCB 1 (a,b), PCB 2 (c,d), and PCB 3 (e,f). Conditions: PCB concentration (7 μM), catalyst weight (10 mg), light power (150 W), pH (neutral), and temperature (20 °C). Control refers to photodegradation of PCBs in the absence of any added material.

reactivity can be attributed to the high surface area of ACOF-1 that can provide numerous active sites. Moreover, Fu *et al.*[31] studied the conformational and electronic details of ACOF-1 using density functional theory (DFT) calculations. They reported that the phenyl and azine groups of ACOF-1 are coplanar, which is an indication for a strong conjugation effect where the LUMO is delocalized through the conjugated π-system of the framework, while the HOMO is localized on the azine linker unit. Fu *et al.*[31] also reported that the HOMO and LUMO energy levels of ACOF-1 are −5.00 and −2.54 eV, respectively, which are large enough to reduce dissolved O_2 to superoxide radicals. To confirm that ACOF-1 is capable of reducing O_2 to superoxide radicals, a set of trapping experiments was conducted using several charge carrier scavengers. In particular, isopropanol (IPA), EDTA, and *p*-benzoquinone (BQ) were used to scavenge hydroxyl radicals, holes, and superoxide radicals, respectively, during the degradation of PCB 1. The data (Figure 6 and Supporting Information, Figure S11) reveal that the addition of isopropanol has almost no effect on the reaction rate, which rules out any probability for the generation of hydroxyl radicals in the system during irradiation of ACOF-1 with light. On the other hand, when EDTA or BQ was added, the degradation

https://doi.org/10.1021/acsanm.0c03425
ACS Appl. Nano Mater. 2021, 4, 2795−2805

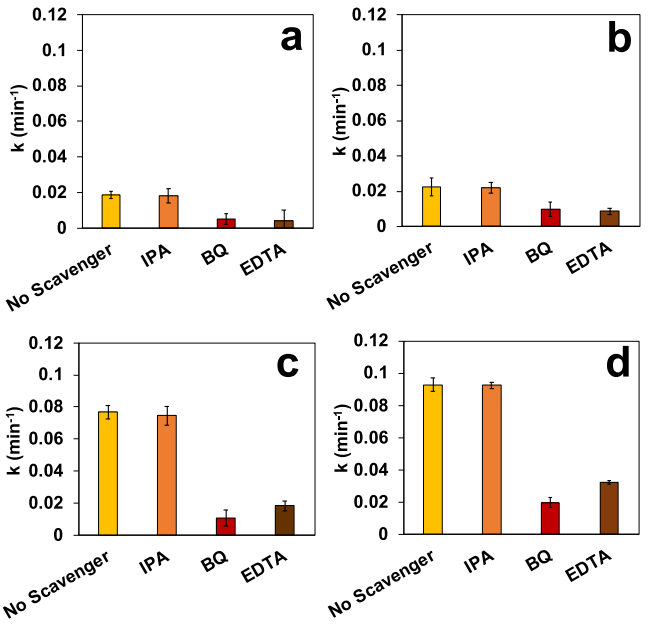

Figure 6. Photocatalytic degradation rate constants of PCB 1 (7 μM) in the presence of isopropanol, *p*-benzoquinone, EDTA, and no scavenger by (a) ACOF-1, (b) ACOF-1@Pd, (c) Cu_2O-ACOF-1, and (d) Cu_2O-ACOF-1@Pd.

rate was drastically reduced. This is evidence that the degradation of PCBs is mainly driven by holes and superoxide radicals, where holes are the dominant species. Overall, photogenerated electrons tend to reduce O_2 because it acts as an electron acceptor and, as a result, superoxide radicals are formed. To investigate further the role of O_2 as an electron acceptor, photocatalytic experiments were conducted in its absence by purging the reaction medium with ultrapure argon before and during the reaction (Supporting Information, Figure S12). The results reveal a substantial decline in the degradation rate similar to the data obtained for BQ trapping experiments, which highlights the crucial role of O_2 in the degradation of PCBs. The data also demonstrate the significance of the photogenerated electrons produced upon the irradiation of ACOF-1.

For ACOF-1@Pd, the degradation rate is notably enhanced upon the decoration of ACOF-1 with Pd nanodomains with degradation extents of 77, 80, and 95% for PCB 1, PCB 2, and PCB 3, respectively, after 60 min of irradiation. It has been reported that the photocatalytic performance of semiconductors could be enhanced upon decoration with noble metal nanodomains because the latter increases the material contact surface while diminishing the electron roaming distance.[22,32] Furthermore, the Fermi level of the metal nanodomains tends to be in equilibrium with the semiconductor conduction band, and that favors the electron transfer to the catalyst surface, thereby enhancing charge separation.[33] The trapping experimental data also support these findings as it is clear that the contribution of superoxide radicals in the system slightly increased upon the decoration of ACOF-1 with Pd nanodomains as displayed in Figure 6b. The deposited nanodomains promote the electron transfer to the O_2 to generate superoxide radicals.

When ACOF-1 was loaded over Cu_2O cubes, the PCB degradation rate increased remarkably with complete degradation being achieved after 50, 50, and 40 min of irradiation for PCB 1, PCB 2, and PCB 3, respectively. Such an increase in the degradation rate can be attributed to the synergy between ACOF-1 and Cu_2O cubes, which enhances the photocatalytic reactivity. It has been reported that the valence and conduction band edge potentials of Cu_2O are −0.6 and 1.4 eV, respectively.[34] Thus, based on the band gap potentials of ACOF-1 mentioned earlier, when Cu_2O-ACOF-1 is irradiated, both ACOF-1 and Cu_2O can be activated; and the photogenerated electrons at the conduction band of ACOF-1 can transfer to that of Cu_2O and finally reach the dissolved O_2 to generate superoxide radicals. The trapping data for Cu_2O-ACOF-1 also support such a hypothesis as the vast majority of the active species within the system became dominated by superoxide radicals. Thus, it can be inferred that the increase in the number of the superoxide radicals by Cu_2O-ACOF-1 can be ascribed to the synergistic effect induced by both of ACOF-1 and Cu_2O upon irradiation with light.

For Cu_2O-ACOF-1@Pd, the degradation rate of the different tested congeners is markedly increased upon the decoration of Cu_2O-ACOF-1 with Pd nanodomains with complete degradation being achieved after 40, 40, and 30 min of irradiation for PCB 1, PCB 2, and PCB 3, respectively, as displayed in Figure 5. Such enhancement in the photocatalytic performance can be ascribed to facilitated electron transfer via the deposited nanodomains to the dissolved O_2 for superoxide radical generation as discussed above. The rate constants obtained for PCB degradation using Cu_2O-ACOF-1@Pd were compared with other reports as listed in Table S1. Specifically, Wang et al.[35] studied the photocatalytic degradation of 2-chlorobiphenyl using TiO_2 and found that TiO_2 enhanced the catalytic degradation of 2-chlorobiphenyl with a rate constant of 0.029 min^{-1}. Zhu et al.[36] also explored the use of TiO_2 in the photocatalytic degradation of 4-chlorobiphenyl and found that TiO_2 was capable of degrading 4-chlorobiphenyl with a rate constant of 0.009 min^{-1}. Pálmai et al.[37] reported that *m*-$BiVO_4$/BiOBr and *m*-$BiVO_4$/BiOBr/Pd were able to degrade 4-chlorobiphenyl with rate constants of 0.014 and 0.03 min^{-1}, respectively. It should be noted that the degradation rates obtained for PCB 1, PCB 2, and PCB 3 using Cu_2O-ACOF-1@Pd with values of 0.092, 0.102, and 0.124 min^{-1}, respectively, emphasize the high impact of using such multicomponent tandem photocatalyst in PCB degradation. Cu_2O cubes were also prepared and decorated with Pd nanodomains for comparison, as shown in Figure 5. It is clear that the degradation rate is lower than that obtained for Cu_2O-ACOF-1@Pd, which highlights the role of ACOF-1 in enhancing the photocatalytic reactivity through a synergy between ACOF-1 and Cu_2O.

To support these findings, electrochemical measurements were conducted for the prepared samples. The electrochemical impedance spectra (EIS) of the prepared samples are displayed in Figure 7a. The size of the semicircle decreases in the order of ACOF-1 > ACOF-1@Pd > Cu_2O-ACOF-1 > Cu_2O-ACOF-1@Pd. Such a decrease can be ascribed to the reduction of charge transfer resistance upon loading of Pd nanodomains and/or Cu_2O cubes, which facilitates the transfer of the photoinduced electrons. The photocurrent measurements were also conducted for the prepared samples, where the obtained data are displayed in Figure 7b. The data reveal that Cu_2O-ACOF-1@Pd exhibits the highest photocurrent generation among the materials tested, which can be attributed to enhanced charge separation.

https://doi.org/10.1021/acsanm.0c03425
ACS Appl. Nano Mater. 2021, 4, 2795−2805

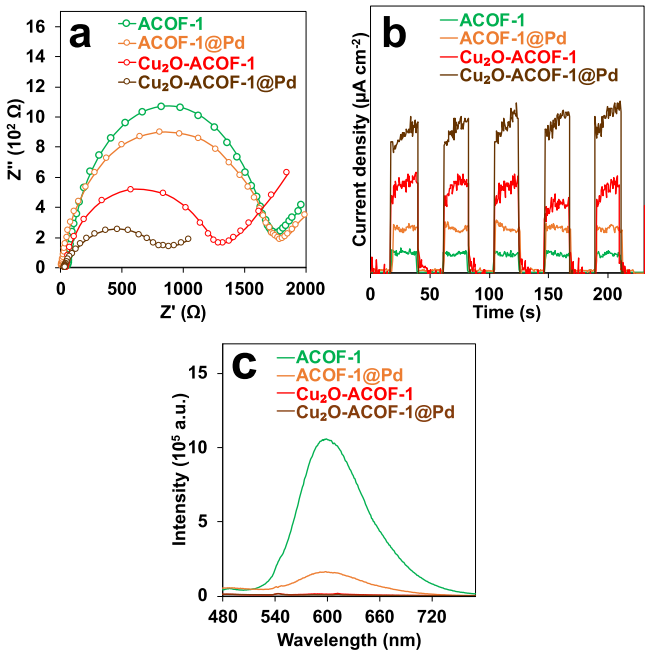

Figure 7. (a) EIS spectra of the prepared materials, (b) transient photocurrent spectra of the prepared materials, and (c) photoluminescence (PL) spectra of the prepared materials.

To investigate the ability of the photocatalyst to enhance charge carrier separation, photoluminescence (PL) analysis was carried out at a wavelength of 400 nm, and the obtained spectra are displayed in Figure 7c. The data reveal that ACOF-1 has a strong emission peak at 600 nm that can be attributed to recombination of the electron−hole pairs. The data also show that the intensity of the emission peak decreased upon loading of Pd nanodomains and Cu_2O cubes. The PL spectrum of Cu_2O-ACOF-1@Pd (Figure S13) exhibits the lowest intensity and thus, it can be inferred that the prepared multicomponent tandem photocatalyst is capable of restraining the recombination of the photogenerated charge carriers.

For all the tested catalysts, the degradation rate of PCB 3 was the highest among the other congeners with a pseudo-first-order rate constant of 0.12 min^{-1} when using Cu_2O-ACOF-1@Pd as the catalyst. The rate constants for photocatalytic degradation of PCBs can be arranged as $(k_{PCB3}) > (k_{PCB2}) > (k_{PCB1})$, and these findings suggest that the PCB congener with a chlorine atom in the para position is more vulnerable to degradation than its meta and ortho counterparts, as it is less sterically hindered. Moreover, the presence of a chlorine atom in the para position increases the conjugation between the phenyl rings, which in turn increases the driving force for planarity that facilitates the removal of the chlorine atom.[38] This photocatalytic trend can be attributed to the reactivity of superoxide radicals toward the different congeners of PCBs. It is worth mentioning that the photogenerated holes can attack nonselectively the organic molecules leading directly to a ring fragmentation. Merritt and Sawyer[39] previously reported that alkyl halides could react with superoxide radicals through a nucleophilic substitution reaction, where the chlorine atom is replaced by superoxide to form peroxy radicals. Kalu and White[40] also reported that electrochemically generated superoxide radicals react with polyhalogenated aromatic hydrocarbons via a nucleophilic substitution reaction. Sugimoto *et al.*[41] studied the reactivity of superoxide radicals with Arochlor 1268, a PCB fraction that consists of a blend of Cl_7, Cl_8, Cl_9, and Cl_{10} PCB congeners, and they found that it was completely degraded in the presence of superoxide radicals. The oxygenation of such compounds could occur via a nucleophilic addition of superoxide that forms a peroxy radical upon the loss of chloride. The formed radical could be reduced by another superoxide radical to form a peroxo nucleophile.[41] Matsunaga *et al.*[42] reported that the reaction of PCB with superoxide with a high rate is the basis behind the absence of low molecular weight aliphatic compounds during PCB oxidation. Moreover, it has been reported that PCB congeners with three or more chlorine atoms per phenyl ring could be entirely degraded using superoxide radicals within hours.[41]

To support this hypothesis, we compared the nucleophilic addition of superoxide radicals for the three congeners using density functional theory (DFT). The calculations were performed on Gaussian 09 program, and the geometry optimization was conducted using the B3LYP/6−31++G(d) level of theory. The optimized structure of the PCB congeners and their corresponding peroxy radicals are presented in the Supporting Information, Figure S14. We propose that the nucleophilic addition of a superoxide radical is followed by elimination of a chloride ion, which gives rise to a biphenyl peroxy radical. Thus, we calculated the rate of nucleophilic substitution reaction for the three congeners, which is the rate-determining step using eq 1,

$$k(T) = \frac{k_B T}{h\, C^0}\, e^{-\Delta G^{\ddagger o}/RT} \quad (1)$$

where k is the rate constant, k_B is the Boltzmann constant, h represents the Planck's constant, C^0 is the concentration, $\Delta G^{\ddagger o}$ is the Gibbs energy of activation, R is the gas constant, and T is temperature in Kelvin. The obtained data (Table 1) reveal that

Table 1. Gibbs Free Energy and Rate Constants Obtained for the Nucleophilic Addition of a Superoxide Radical

congener	$\Delta G^{\ddagger o}$ (kcal mol^{-1})	k (s^{-1})
PCB 1	7.12	3.69×10^7
PCB 2	7.07	4.06×10^7
PCB 3	6.84	5.94×10^7

the rate constant follows the order: $k_{PCB3} > k_{PCB2} > k_{PCB1}$, which means that the chlorine atom in the para position is more vulnerable to substitution by superoxide than its meta and ortho counterparts. Moreover, the value of Gibbs free energy for para-substituted PCB is 6.84 kcal mol^{-1}, while for the meta and ortho counterparts, the corresponding values are 7.07 and 7.12 kcal mol^{-1}, respectively. Indeed, the nucleophilic substitution occurring at the para position is characterized by the lowest Gibbs free energy, while the nucleophilic substitution occurring at the ortho position is characterized by the highest Gibbs free energy.

Furthermore, TOC analysis was used to estimate the extent of mineralization after the degradation of the three congeners using Cu_2O-ACOF-1@Pd, and the obtained data are displayed in Figure S15. The results revealed an appreciable decrease in the total organic carbon content after 60 min of irradiation with TOC removals of 95.0, 86.6, and 67.2%, for PCB 3, PCB 2, and PCB 1, respectively. Such results emphasize the ability of the employed system to mineralize the three congeners into carbon dioxide and water.[43] Moreover, these findings suggest that the mineralization of the three congeners is dependent on

https://doi.org/10.1021/acsanm.0c03425
ACS Appl. Nano Mater. 2021, 4, 2795−2805

the chlorine position, which markedly affects the photocatalytic activity based on steric hindrance and electronic effects.

To screen the effect of catalyst amount on the photocatalytic degradation of PCB 3, a set of experiments was conducted using different amounts of Cu_2O-ACOF-1@Pd, and the obtained data are presented in the Supporting Information, Figure S16. As expected, the degradation rate exhibits an increase upon increasing the catalyst amount as a result of more active sites becoming available, which amplifies the number of produced reactive species. However, the increase in the degradation rate was not linear with the amount of the catalyst added. For 20 mg of Cu_2O-ACOF-1@Pd, which is twofold higher than the 10 mg case, the degradation rate increased by only 41%, while for the 40 mg of Cu_2O-ACOF-1@Pd (fourfold increase), the degradation rate increased by 55%. This dissipation can be attributed to the obstruction of light absorption by the excessive amount of catalyst particles, where some particles mask the light from illuminating the neighboring particles. Thus, the amount of the catalyst should be optimized to provide maximum efficiency. The light power is another parameter that influences the degradation rate of organic contaminants. The impact of light power on the degradation of PCB 3 was also studied, and the results are displayed in the Supporting Information, Figure S17. The degradation rate of PCB 3 exhibits an increase that is directly proportional to the light power, where complete degradation of PCB 3 was achieved after only 15 min of irradiation using a power of 300 W.

As sustainability becomes an increasingly pressing priority in wastewater treatment, photocatalysts with a minimal ecological impact are being sought out. Thus, researchers aspire to develop a photocatalyst that can endure harsh conditions so that it can be reused over many catalytic cycles. To evaluate the endurance of the prepared Cu_2O-ACOF-1@Pd, the photocatalytic degradation of PCB 3 was conducted with the same recovered catalyst using the same parameters for four consecutive runs. After each experiment, Cu_2O-ACOF-1@Pd was separated from the reaction mixture and dried. For the first run, the complete degradation of PCB 3 was achieved after 30 min, and for the fourth run, 97% of PCB 3 was degraded after 30 min of irradiation (Supporting Information, Figure S18). To assure the stability of the photocatalyst during the degradation of PCB 3, the recovered catalyst was analyzed using XRD and FTIR, and it was found that there is no noticeable difference in the XRD pattern and FTIR spectrum of the recovered catalyst (Supporting Information, Figure S19). Thus, it can be concluded that the employed Cu_2O-ACOF-1@Pd is able to sustain the experimental conditions during the photocatalytic degradation of PCBs.

CONCLUSIONS

In conclusion, Cu_2O cubes decorated with azine-based covalent organic framework spheres and Pd nanoparticles exhibit the best performance among the other tested catalysts, where complete degradation of PCB 1, PCB 2, and PCB 3 was observed in very short timescales. This outstanding performance can be attributed to the synergistic effect induced by the multicomponent tandem photocatalyst. For all the tested catalysts, the degradation rate of PCB 3 was the highest among the other congeners. The rate constants for photocatalytic degradation of PCBs can be arranged as $(k_{PCB3}) > (k_{PCB2}) > (k_{PCB1})$, and these findings suggest that the PCB congener with chlorine in the para position is more vulnerable to degradation than its meta and ortho counterparts. This trend is attributed to the reactivity of superoxide radicals toward the different congeners of PCBs. We propose that oxygenation of PCBs could occur via a nucleophilic addition of superoxide radicals that forms a peroxy radical upon the loss of a chloride ion. Accordingly, we calculated the rate of the nucleophilic substitution reaction using DFT for the three congeners and found that the rate constant mirrors the observed experimental results, confirming that the chlorine atom in the para position is more vulnerable to be substituted by a superoxide radical than the meta and ortho counterparts.

ASSOCIATED CONTENT

Supporting Information

The Supporting Information is available free of charge at https://pubs.acs.org/doi/10.1021/acsanm.0c03425.

Ultrasonic-assisted preparation of ACOF-1; FTIR spectra of 1,3,5-triformylbenzene and ACOF-1; ^{13}C CP/MAS NMR spectroscopy of 1,3,5-triformylbenzene and ACOF-1; XRD patterns of the prepared materials; N_2 adsorption−desorption isotherm of the prepared materials; absorption spectrum of ACOF-1 and plot of $(\alpha h\nu)^2$ vs energy and $(\alpha h\nu)^{1/2}$ vs energy in the absorption edge region for ACOF-1; TEM images of ACOF-1@Pd and Cu_2O@Pd; SEM images of Cu_2O-ACOF-1 prepared by physical mixing of Cu_2O and ACOF-1; FTIR analysis of the prepared materials; absorption spectrum of Cu_2O and plot of $(\alpha h\nu)^2$ vs energy and $(\alpha h\nu)^{1/2}$ vs energy in the absorption edge region for Cu_2O; adsorption of PCB 1, PCB 2, and PCB 3; photocatalytic degradation of PCB 1 in the presence of radical scavengers; Ar-purged photocatalytic degradation and pseudo-first-order rate constants of PCB 1; PL spectra of Cu_2O-ACOF-1 and Cu_2O-ACOF-1@Pd; optimized structures calculated using a DFT method at the B3LYP/6−31++G(d) level for PCB 1, PCB 2, and PCB 3; TOC removal of PCB 1, PCB 2 and PCB 3 using Cu_2O-ACOF-1@Pd; effect of the catalyst amount on the photocatalytic degradation and pseudo-first-order rate constants of PCB 3; effect of light power on the photocatalytic degradation and pseudo-first-order rate constants of PCB 3; reusability of Cu_2O-ACOF-1@Pd in the photocatalytic degradation of PCB 3; XRD pattern and FTIR curve of Cu_2O-ACOF-1@Pd after the photocatalytic degradation of PCB 3; and comparison of the rate constants obtained for Cu_2O-ACOF-1@Pd with other reports (PDF)

AUTHOR INFORMATION

Corresponding Author

Leonidas G. Bachas − *Department of Chemistry and Dr. J.T. Macdonald Foundation Biomedical Nanotechnology Institute, University of Miami, Coral Gables, Florida 33146, United States;* orcid.org/0000-0002-3308-6264; Email: bachas@miami.edu

Authors

Ahmed E. ElMetwally − *Department of Chemistry, University of Miami, Coral Gables, Florida 33146, United States;* orcid.org/0000-0001-6746-6372

Elnaz Zeynaloo − *Department of Chemistry, University of Miami, Coral Gables, Florida 33146, United States;* orcid.org/0000-0001-7152-5857

Dharmendra Shukla − *Department of Physics, University of Miami, Coral Gables, Florida 33146, United States*

Bapurao Surnar − *Department of Biochemistry and Molecular Biology, Leonard M. Miller School of Medicine, University of Miami, Miami, Florida 33136, United States;* orcid.org/0000-0001-5997-3120

Shanta Dhar − *Department of Biochemistry and Molecular Biology, Leonard M. Miller School of Medicine, University of Miami, Miami, Florida 33136, United States;* orcid.org/0000-0003-3042-5272

Joshua L. Cohn − *Department of Physics, University of Miami, Coral Gables, Florida 33146, United States;* orcid.org/0000-0002-0702-9872

Marc R. Knecht − *Department of Chemistry and Dr. J.T. Macdonald Foundation Biomedical Nanotechnology Institute, University of Miami, Coral Gables, Florida 33146, United States;* orcid.org/0000-0002-7614-7258

Complete contact information is available at: https://pubs.acs.org/10.1021/acsanm.0c03425

Author Contributions

All authors have given approval to the final version of the manuscript.

Notes

The authors declare no competing financial interest.

■ ACKNOWLEDGMENTS

Financial support by the University of Miami is gratefully acknowledged. XRD studies (D.S. and J.L.C.) were supported by the U.S. Department of Energy (DOE), Office of Science, Basic Energy Sciences (BES), under award no. DE-SC0008607.

■ REFERENCES

(1) Afghan, B.; Chau, A. S. *Analysis of Trace Organics in the Aquatic Environment;* CRC press, 1989.

(2) Liu, Y.; Wang, S.; McDonough, C. A.; Khairy, M.; Muir, D. C. G.; Helm, P. A.; Lohmann, R. Gaseous and Freely-Dissolved PCBs in the Lower Great Lakes Based on Passive Sampling: Spatial Trends and Air−Water Exchange. *Environ. Sci. Technol.* **2016**, *50*, 4932−4939.

(3) Ullah, R.; Asghar, R.; Baqar, M.; Mahmood, A.; Alamdar, A.; Qadir, A.; Sohail, M.; Schäfer, R. B.; Musstjab Akber Shah Eqani, S. A. Assessment of Polychlorinated Biphenyls (PCBs) in the Himalayan Riverine Network of Azad Jammu and Kashmir. *Chemosphere* **2020**, *240*, 124762.

(4) Marek, R. F.; Thorne, P. S.; Herkert, N. J.; Awad, A. M.; Hornbuckle, K. C. Airborne PCBs and OH-PCBs Inside and Outside Urban and Rural U.S. Schools. *Environ. Sci. Technol.* **2017**, *51*, 7853−7860.

(5) Khammar, S.; Bahramifar, N.; Younesi, H. Preparation and Surface Engineering of CM-B-CD Functionalized Fe_3O_4@TiO_2 Nanoparticles for Photocatalytic Degradation of Polychlorinated Biphenyls (PCBs) from Transformer Oil. *J. Hazard. Mater.* **2020**, *394*, 122422.

(6) Schröder, S.; San-Román, M.-F.; Ortiz, I. Dioxins and Furans Toxicity During the Photocatalytic Remediation of Emerging Pollutants. Triclosan as Case Study. *Sci. Total Environ.* **2021**, *770*, 144853.

(7) Côté, A. P.; Benin, A. I.; Ockwig, N. W.; O'Keeffe, M.; Matzger, A. J.; Yaghi, O. M. Porous, Crystalline, Covalent Organic Frameworks. *Science* **2005**, *310*, 1166.

(8) Liu, R.; Tan, K. T.; Gong, Y.; Chen, Y.; Li, Z.; Xie, S.; He, T.; Lu, Z.; Yang, H.; Jiang, D. Covalent Organic Frameworks: An Ideal Platform for Designing Ordered Materials and Advanced Applications. *Chem. Soc. Rev.* **2021**, *50*, 120−242.

(9) Dalapati, S.; Jin, S.; Gao, J.; Xu, Y.; Nagai, A.; Jiang, D. An Azine-Linked Covalent Organic Framework. *J. Am. Chem. Soc.* **2013**, *135*, 17310−17313.

(10) Chandra, S.; Kundu, T.; Kandambeth, S.; BabaRao, R.; Marathe, Y.; Kunjir, S. M.; Banerjee, R. Phosphoric Acid Loaded Azo (−N═N−) Based Covalent Organic Framework for Proton Conduction. *J. Am. Chem. Soc.* **2014**, *136*, 6570−6573.

(11) Fang, Q.; Wang, J.; Gu, S.; Kaspar, R. B.; Zhuang, Z.; Zheng, J.; Guo, H.; Qiu, S.; Yan, Y. 3D Porous Crystalline Polyimide Covalent Organic Frameworks for Drug Delivery. *J. Am. Chem. Soc.* **2015**, *137*, 8352−8355.

(12) DeBlase, C. R.; Silberstein, K. E.; Truong, T.-T.; Abruña, H. D.; Dichtel, W. R. *β*-Ketoenamine-Linked Covalent Organic Frameworks Capable of Pseudocapacitive Energy Storage. *J. Am. Chem. Soc.* **2013**, *135*, 16821−16824.

(13) van der Jagt, R.; Vasileiadis, A.; Veldhuizen, H.; Shao, P.; Feng, X.; Ganapathy, S.; Habisreutinger, N. C.; van der Veen, M. A.; Wang, C.; Wagemaker, M.; van der Zwaag, S.; Nagai, A. Synthesis and Structure−Property Relationships of Polyimide Covalent Organic Frameworks for Carbon Dioxide Capture and (Aqueous) Sodium-Ion Batteries. *Chem. Mater.* **2021**, *33*, 818−833.

(14) Feng, K.; Hao, H.; Huang, F.; Lang, X.; Wang, C. A 2D Porphyrin-Based Covalent Organic Framework with TEMPO for Cooperative Photocatalysis in Selective Aerobic Oxidation of Sulfides. *Mater. Chem. Front.* **2021**, 2255.

(15) Vyas, V. S.; Lau, V. W.-h.; Lotsch, B. V. Soft Photocatalysis: Organic Polymers for Solar Fuel Production. *Chem. Mater.* **2016**, *28*, 5191−5204.

(16) Kuecken, S.; Acharjya, A.; Zhi, L.; Schwarze, M.; Schomäcker, R.; Thomas, A. Fast Tuning of Covalent Triazine Frameworks for Photocatalytic Hydrogen Evolution. *Chem. Commun.* **2017**, *53*, 5854−5857.

(17) Bi, J.; Fang, W.; Li, L.; Wang, J.; Liang, S.; He, Y.; Liu, M.; Wu, L. Covalent Triazine-Based Frameworks as Visible Light Photocatalysts for the Splitting of Water. *Macromol. Rapid Commun.* **2015**, *36*, 1799−1805.

(18) Lin, S.; Diercks, C. S.; Zhang, Y.-B.; Kornienko, N.; Nichols, E. M.; Zhao, Y.; Paris, A. R.; Kim, D.; Yang, P.; Yaghi, O. M.; Chang, C. J. Covalent Organic Frameworks Comprising Cobalt Porphyrins for Catalytic CO_2 Reduction in Water. *Science* **2015**, *349*, 1208.

(19) Li, L.; Fang, W.; Zhang, P.; Bi, J.; He, Y.; Wang, J.; Su, W. Sulfur-Doped Covalent Triazine-Based Frameworks for Enhanced Photocatalytic Hydrogen Evolution from Water Under Visible Light. *J. Mater. Chem. A* **2016**, *4*, 12402−12406.

(20) Thote, J.; Aiyappa, H. B.; Deshpande, A.; Dïaz Dïaz, D.; Kurungot, S.; Banerjee, R. A Covalent Organic Framework−Cadmium Sulfide Hybrid as a Prototype Photocatalyst for Visible-Light-Driven Hydrogen Production. *Chem. - Eur. J.* **2014**, *20*, 15961−15965.

(21) Li, Z.; Feng, X.; Zou, Y.; Zhang, Y.; Xia, H.; Liu, X.; Mu, Y. A 2D Azine-Linked Covalent Organic Framework for Gas Storage Applications. *Chem. Commun.* **2014**, *50*, 13825−13828.

(22) Zahran, E. M.; Bedford, N. M.; Nguyen, M. A.; Chang, Y.-J.; Guiton, B. S.; Naik, R. R.; Bachas, L. G.; Knecht, M. R. Light-Activated Tandem Catalysis Driven by Multicomponent Nanomaterials. *J. Am. Chem. Soc.* **2014**, *136*, 32−35.

(23) Zhang, K.-L.; Liu, C.-M.; Huang, F.-Q.; Zheng, C.; Wang, W.-D. Study of the Electronic Structure and Photocatalytic Activity of the BiOCl Photocatalyst. *Appl. Catal., B* **2006**, *68*, 125−129.

(24) ElShafei, G. M. S.; Al-Sabagh, A. M.; Yehia, F. Z.; Philip, C. A.; Moussa, N. A.; Eshaq, G.; ElMetwally, A. E. Metal Oxychlorides as Robust Heterogeneous Fenton Catalysts for the Sonophotocatalytic Degradation of 2-Nitrophenol. *Appl. Catal., B* **2018**, *224*, 681−691.

(25) ElMetwally, A. E.; Eshaq, G.; Al-Sabagh, A. M.; Yehia, F. Z.; Philip, C. A.; Moussa, N. A.; ElShafei, G. M. S. Insight into

Heterogeneous Fenton-Sonophotocatalytic Degradation of Nitrobenzene using Metal Oxychlorides. *Sep. Purif. Technol.* **2019**, *210*, 452−462.
(26) Nguyen, M. A.; Zahran, E. M.; Wilbon, A. S.; Besmer, A. V.; Cendan, V. J.; Ranson, W. A.; Lawrence, R. L.; Cohn, J. L.; Bachas, L. G.; Knecht, M. R. Converting Light Energy to Chemical Energy: A New Catalytic Approach for Sustainable Environmental Remediation. *ACS Omega* **2016**, *1*, 41−51.
(27) Solomon, J. L.; Madix, R. J.; Stöhr, J. Orientation and Absolute Coverage of Benzene, Aniline, and Phenol on Ag(110) Determined by NEXAFS and XPS. *Surf. Sci.* **1991**, *255*, 12−30.
(28) Wei, X.-L.; Fahlman, M.; Epstein, A. J. XPS Study of Highly Sulfonated Polyaniline. *Macromolecules* **1999**, *32*, 3114−3117.
(29) Wang, W. Z.; Wang, G. H.; Wang, X. S.; Zhan, Y. J.; Liu, Y. K.; Zheng, C. L. Synthesis and Characterization of Cu_2O Nanowires by a Novel Reduction Route. *Adv. Mater.* **2002**, *14*, 67−69.
(30) Wang, Y.; Lü, Y.; Zhan, W.; Xie, Z.; Kuang, Q.; Zheng, L. Synthesis of Porous Cu_2O/CuO Cages Using Cu-Based Metal−Organic Frameworks as Templates and Their Gas-Sensing Properties. *J. Mater. Chem. A* **2015**, *3*, 12796−12803.
(31) Fu, Y.; Zhu, X.; Huang, L.; Zhang, X.; Zhang, F.; Zhu, W. Azine-Based Covalent Organic Frameworks as Metal-Free Visible Light Photocatalysts for CO_2 Reduction with H_2O. *Appl. Catal., B* **2018**, *239*, 46−51.
(32) Jia, Y.; Shen, S.; Wang, D.; Wang, X.; Shi, J.; Zhang, F.; Han, H.; Li, C. Composite Sr_2TiO_4/$SrTiO_3$(La,Cr) Heterojunction Based Photocatalyst for Hydrogen Production Under Visible Light Irradiation. *J. Mater. Chem. A* **2013**, *1*, 7905−7912.
(33) Subramanian, V.; Wolf, E. E.; Kamat, P. V. Catalysis with TiO_2/Gold Nanocomposites. Effect of Metal Particle Size on the Fermi Level Equilibration. *J. Am. Chem. Soc.* **2004**, *126*, 4943−4950.
(34) Eshaq, G.; ElMetwally, A. E. Bmim[OAc]-Cu_2O/g-C_3N_4 as a Multi-Function Catalyst for Sonophotocatalytic Degradation of Methylene Blue. *Ultrason. Sonochem.* **2019**, *53*, 99−109.
(35) Wang, Y.; Hong, C.-S.; Fang, F. Effect of Solution Matrix on TiO_2 Photocatalytic Degradation of 2-Chlorobiphenyl. *Environ. Eng. Sci.* **1999**, *16*, 433−440.
(36) Zhu, X.; Zhou, D.; Cang, L.; Wang, Y. TiO_2 Photocatalytic Degradation of 4-Chlorobiphenyl as Affected by Solvents and Surfactants. *J. Soils Sediments* **2012**, *12*, 376−385.
(37) Pálmai, M.; Zahran, E. M.; Angaramo, S.; Bálint, S.; Pászti, Z.; Knecht, M. R.; Bachas, L. G. Pd-Decorated *m*-$BiVO_4$/BiOBr Ternary Composite with Dual Heterojunction for Enhanced Photocatalytic Activity. *J. Mater. Chem. A* **2017**, *5*, 529−534.
(38) Ruzo, L. O.; Zabik, M. J.; Schuetz, R. D. Photochemistry of Bioactive Compounds. Photochemical Processes of Polychlorinated Biphenyls. *J. Am. Chem. Soc.* **1974**, *96*, 3809−3813.
(39) Merritt, M. V.; Sawyer, D. T. Electrochemical Studies of the Reactivity of Superoxide Ion with Several Alkyl Halides in Dimethyl Sulfoxide. *J. Org. Chem.* **1970**, *35*, 2157−2159.
(40) Kalu, E. E.; White, R. E. *In Situ* Degradation of Polyhalogenated Aromatic Hydrocarbons by Electrochemically Generated Superoxide Ions. *J. Electrochem. Soc.* **1991**, *138*, 3656−3660.
(41) Sugimoto, H.; Matsumoto, S.; Sawyer, D. T. Oxygenation of Polychloro Aromatic Hydrocarbons by Superoxide Ion in Aprotic Media. *J. Am. Chem. Soc.* **1987**, *109*, 8081−8082.
(42) Matsunaga, K.; Imanaka, M.; Kenmotsu, K.; Hino, S.; Kadota, M.; Fujiwara, H.; Mori, T. Superoxide Radical-Induced Degradation of Polychlorobiphenyls and Chlordanes at Low Temperature (Proceedings of the 14th Symposium on Environmental Pollutants and Toxicology). *Eisei kagaku* **1989**, *35*, P2−P2.
(43) Chi, G. T.; Huddersman, K. D. Maleic Acid Oxidation Using a Heterogeneous Modified Polyacrylonitrile (PAN) Fibrous Catalyst. *J. Adv. Oxid. Technol.* **2011**, *14*, 235−243.

https://doi.org/10.1021/acsanm.0c03425
ACS Appl. Nano Mater. 2021, 4, 2795−2805